PAPER

Check for updates

Tailored design of *p*-phenylenediamine functionalized graphene decorated with cobalt ferrite for microwave absorption

Tao Ma, †[a] Yu Cui,†[b] Li Liu,*[a] Hao Luan,[a] Jianwen Ge,[a] Pengfei Ju,[c] Fandi Meng[a] and Fuhui Wang[a]

Structural design and componental optimization are two primary directions in the study of microwave absorbers. In this study, a novel cobalt ferrite ($CoFe_2O_4$) decorated with *p*-phenylenediamine (PPD) functionalized graphene ($PG/CoFe_2O_4$) binary hybrid with unique hierarchical porous structure was synthesized by a two-step route. The chemical composition, morphology and electromagnetic parameters of the as-prepared sample were investigated successively. The porous $CoFe_2O_4$ microspheres with an average diameter of about 160 nm were uniformly anchored on rGO nanosheets. Owing to the uniquely hierarchical porous structure, synergistic effects of dielectric loss (conductive loss, interface and dipole polarization) and magnetic loss (eddy current loss, natural and exchange resonance), the as-prepared sample exhibited excellent microwave absorption (MA) performance. The maximum reflection loss (RL_{max}) could attain up to −53.3 dB, and the effective absorption bandwidth (EAB) reached 6.6 GHz (11.4–18.0 GHz) at 2.40 mm, which completely covered the K_u band. These results showed that this functional material can be applied in the MA field.

1. Introduction

In order to address the problems of microwave radiation and interference arising from the widespread use of electronic devices and equipment, it is urgent to design high-performance MA materials with the traits of light weight, thin thickness, strong absorption and wide bandwidth.[1–3]

Graphene has drawn considerable attention in the MA field owing to its low density, large specific surface area and strong dielectric loss.[4,5] However, pure graphene usually leads to bad impedance matching and weak absorption due to its high conductivity.[6,7] Fortunately, the large specific surface endow it with the ability to load various particles. Hence, scholars have been dedicated to combining graphene with magnetic particles to integrate the advantages of dielectric and magnetic materials over last few years.[8–10] To further achieve moderate impedance matching and attenuation capacity, different reductants and dopants were employed to fabricate graphene-based absorbers. For instance, FeNi/N-GN (hydrazine hydrate as reductant and dopant),[11] $Co_{0.8}Fe_{2.2}O_4$/rGO (sodium borohydride as reductant),[12] FeCo/N-doped carbon/rGO (ascorbic acid),[13] graphene/Fe_3O_4@-PPy (ethylenediamine)[14] and rGO/MWCNTs/$ZnFe_2O_4$ (glucose).[15]

In addition, it is reported that GO reduced and functionalized by PPD can form cross-linked graphene networks to greatly enhance the conductivity and increase the layer spacing to prevent restacking and aggregation.[16,17] Furthermore, functional groups containing nitrogen introduced into graphene can produce defect and dipole polarization, which will conduce to MA.[18–20] So it may have potential to act as a new-style dielectric material used in MA field by loading with magnetic component.

Compared to other spinel ferrites, cobalt ferrite shows high magnetic loss due to its higher saturation magnetization and magnetic anisotropy.[21–23] Thus it has been widely studied as competitive candidates for absorber. For example, $CoFe_2O_4$@1T/2H-MoS_2,[24] $CoFe_2O_4$-Ti_3C_2,[23] $CoFe_2O_4$/CNFs,[25] C@$CoFe_2O_4$,[26] and CF@$CoFe_2O_4$@MnO_2.[27] From above research, it is not hard to notice that $CoFe_2O_4$ was decorated with various dielectric materials to prepare high-performance absorbers. Besides, rational structure design is another way to prepare high-efficiency absorber. Among all structures, porous structure exhibits the superiority of light-weight and enhanced microwave attenuation.[11] Hence, combining graphene with porous $CoFe_2O_4$ could be a reasonable design for MA.

Herein, we successfully synthesized hierarchical porous PG/$CoFe_2O_4$ binary hybrid by using PPD to functionalize and reduce GO. The PG/$CoFe_2O_4$ exhibited excellent MA performance than pure $CoFe_2O_4$. The optimal RL could reach up to −53.3 dB. The EAB attained 6.6 GHz (from 11.4 to 18.0 GHz) at 2.40 mm, covering the whole K_u band. Thus, the binary composite has great potential to be applied as newly high-performance absorber.

[a]*Shenyang National Laboratory for Materials Science, Northeastern University, Shenyang 110819, China. E-mail: liuli@mail.neu.edu.cn*
[b]*Institute of Metal Research, Chinese Academy of Sciences, Shenyang 110016, China*
[c]*Shanghai Aerospace Equipment Manufacture, Shanghai 200245, China*
† Contributed to this work equally.

2. Experimental

2.1 Materials

Graphite oxide (GO) was supplied by Shenzhen Matterene Tech Co., Ltd (Shenzhen, China). Ferric chloride hexahydrate ($FeCl_3 \cdot 6H_2O$), cobalt chloride hexahydrate ($CoCl_2 \cdot 6H_2O$), urea, ethylene glycol, diglycol, polyvinylpyrrolidone (PVP, K30), ammonium hydroxide and ethanol were obtained from Sinopharm Chemical Reagent, China. And p-phenylenediamine was bought from Aladdin Bio-Chem Technology Co., Ltd, Shanghai, China. Deionized water was used throughout the experiments.

2.2 Synthesis of PG/CoFe₂O₄ composite

Firstly, the $CoFe_2O_4$ was fabricated by a solvothermal method according to our previous report with some modification.[28] In a typical procedure, $FeCl_3 \cdot 6H_2O$ (5 mmol), $CoCl_2 \cdot 6H_2O$ (2.5 mmol) and polyvinylpyrrolidone (K30, 0.2 g) were dissolved into 40 mL mixed solution containing same-volumetric ethylene glycol and diglycol with magnetic stirring for 40 min, then urea (40 mmol) was added. The mixture solution was sealed into Teflon-lined autoclave (50 mL) and maintained in 180 °C for 20 h. The $CoFe_2O_4$ was obtained. Secondly, the above as-prepared $CoFe_2O_4$ (500 mg) were dispersed in 100 mL 2 mg mL^{-1} GO aqueous solution with ultrasonically treating for 60 min. Afterwards, p-phenylenediamine (2.0 g) and ammonium hydroxide (0.6 mL) was added with further stirring for 5 h at 95 °C in oil bath pot. Finally, the PG/CoFe₂O₄ composite was obtained by filtrated, washed and dried. The pure PG was synthesized under the same conditions except for the addition of $CoFe_2O_4$.

2.3 Characterization

The structure, morphology and electromagnetic parameters of the samples were measured by X-ray diffraction (XRD, Rigaku, Cu-K$_\alpha$), Fourier transform infrared spectroscopy (FT-IR, BRUKER, VERTEX70), Raman spectra (HORIBA, XPLORA), X-ray photoelectron spectrometer (XPS, Thermo VG, ESCA-LAB250), scanning electron microscopy (SEM, JEOL, JSM-7001F), transmission electron microscopy (TEM, JEOL, JEM-2100F), energy dispersive X-ray spectroscopy (EDS) and vector network analyzer (Agilent E5071C), respectively. The specimens of electromagnetic parameters were tested by mixing samples with paraffin by the mass ratio of 1 : 1, and then pressed into toroidal shape of $\varphi_{out} = 7.00$ mm and $\varphi_{in} = 3.04$ mm with a thickness of 2.0 mm.

3. Results and discussion

The synthetic route of PG/CoFe₂O₄ composite is schematically represented in Fig. 1a. Firstly, porous $CoFe_2O_4$ were prepared by solvothermal process with the help of surfactant PVP. Then, the $CoFe_2O_4$ microspheres were loaded on the surface of GO nanosheets under electrostatic interaction. Finally, the amine of PPD was reacted with epoxy group and carboxyl group of GO through nucleophilic substitution and condensation reaction.[17,29] The GO was reduced and functionalized and PG/CoFe₂O₄ binary hybrid was prepared.

The XRD patterns of PG, $CoFe_2O_4$ and PG/CoFe₂O₄ composite are shown in Fig. 1b. The PG exhibits a broad characteristic peak at around 20.8° instead of 11° (graphene oxide), indicating that GO was reduced to PG with the presence of p-phenylenediamine. For $CoFe_2O_4$, the diffraction peaks are obtained at 18.3°, 30.1°, 35.4°, 43.1°, 53.5°, 57.0° and 62.6°, which assign to the (111), (220), (311), (400), (422), (511) and (440) planes of $CoFe_2O_4$ (JCPDS card no. 22-1086).[24] The peaks of PG/CoFe₂O₄ composite are nearly the same with $CoFe_2O_4$. In addition, the characteristic peak of PG is disappeared, which is
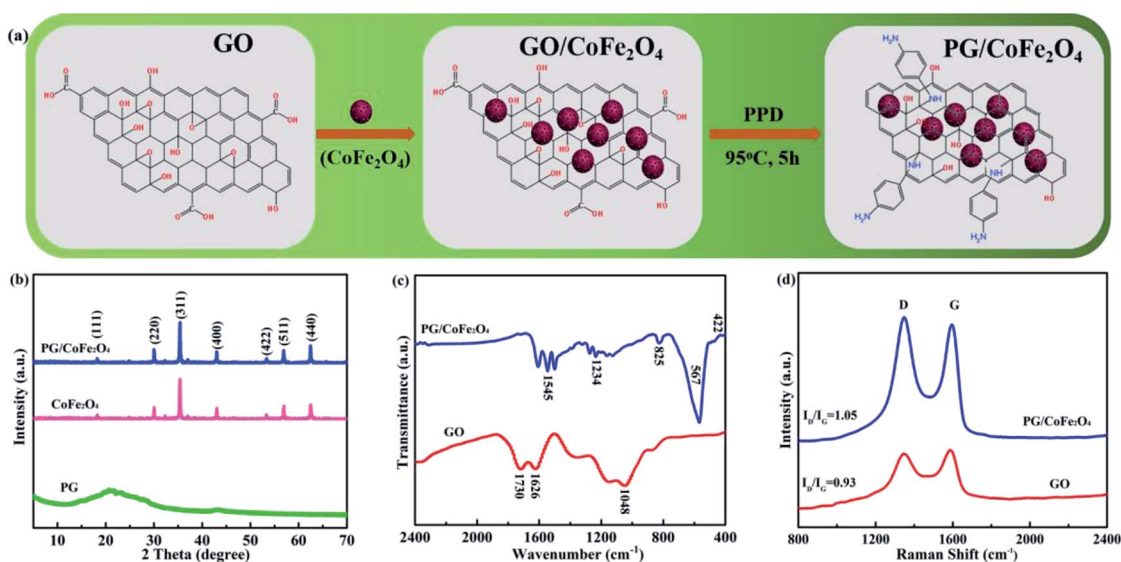

Fig. 1 (a) Synthetic route of PG/CoFe₂O₄ composite, (b) XRD patterns of PG, CoFe₂O₄ and PG/CoFe₂O₄ composite, (c) FT-IR spectra and (d) Raman spectra of GO and PG/CoFe₂O₄ composite.

on account of PG layers were separated by interbedded $CoFe_2O_4$ to avoid stacking.[30]

Fig. 1c shows FT-IR spectra of GO and PG/$CoFe_2O_4$ composite. The GO exhibits four distinct characteristic peaks at 1730 cm^{-1} (C=O in carboxyl group), 1626 cm^{-1} (C=C in aromatic ring) and 1048 cm^{-1} (C–O in epoxide group).[31] For PG/$CoFe_2O_4$ composite, the peaks corresponding to epoxide and carboxyl group weaken or vanish. Meanwhile, three new peaks are detected at 1545 cm^{-1}, 1234 cm^{-1} and 825 cm^{-1} assigning to the stretching vibration of N–H in –C–NH$_2$ groups, stretching vibration of C–N in C–NH–C bonds and asymmetric 1,4-substituent of benzene ring.[32] All the results imply that the epoxide and carboxyl groups of GO were reacted with the amine group of PPD to form PG effectively. In addition, another two new peaks at 567 cm^{-1} and 422 cm^{-1} associated with vibrations of Fe–O and Co–O bonds further indicate the presence of $CoFe_2O_4$.

Fig. 1d presents Raman spectra of GO and PG/$CoFe_2O_4$ composite. It can be observed that both samples present two distinct peaks called D band (1349 cm^{-1}) and G band (1591 cm^{-1}), relating to the vibration of sp^3 defects and the disorder sites and in-plane sp^2 hybridization. Moreover, the intensity of I_D/I_G is usually used to characterize the defects and disorders of carbon materials. The I_D/I_G of PG/$CoFe_2O_4$ is 1.05, which is higher than that of GO (0.93). It suggests that the introduction of PPD can destroy the ordered sp^2 domains and generate more defects and disorders in PG/$CoFe_2O_4$ composite, further it will contribute to microwave absorption.[33]

The element composition and formation of chemical bond of GO and PG was analyzed by XPS. The survey spectra of GO and PG are shown in Fig. 2a. The GO presents two peaks of C 1s and O 1s. After functionalized by PPD, there exists a new peak of N 1s for PG. Meanwhile, the oxygen amount was reduced from 31.72% (GO) to 7.90% (PG). The high-resolution C 1s spectra of GO and PG are exhibited in Fig. 2b and c, respectively. For GO, it can be fitted into four peaks at 284.4, 286.3, 287.0 and 288.3 eV, assigning to the groups of C–C/C=C (aromatic rings), C–OH (hydroxyl), C–O–C (epoxy) and C–O=C (carboxyl), respectively. As for PG, the peaks corresponding to epoxide and carboxyl groups disappear and a new peak appears at 285.6 eV ascribed to C–N group. The results further confirm that the

epoxide and carboxyl groups of GO were reacted with the amine group of PPD.

The morphology and microstructure of $CoFe_2O_4$ and PG/$CoFe_2O_4$ composite are investigated by SEM and TEM, as shown in Fig. 3. In Fig. 3a–c, the $CoFe_2O_4$ presents a spherical shape and the average diameter of about 160 nm. Moreover, it exhibits an uneven surface and a mass of nano-holes are well distributed in $CoFe_2O_4$ microparticle. This porous structure not only decreases the density but also optimizes impedance matching. Besides, it can induce plentiful interfaces and to generate interfacial polarization and multiple reflection.[34] For PG/$CoFe_2O_4$ (Fig. 3d and e), the wrinkled and transparent sheets are supposed to PG (marked in blue arrow) and porous $CoFe_2O_4$ particles (marked in red arrow) are uniformly embedded in the surface of PG to prevent restacking. In Fig. 3f, the HRTEM image shows the lattice spacing of 0.29 nm, assigning to the (220) plane of $CoFe_2O_4$. And this result is in consistent with XRD and FT-IR characterizations. The elemental mapping analysis (Fig. 3g) shows that PG/$CoFe_2O_4$ composite consists of Co, Fe, O, C and N elements. It indicates that $CoFe_2O_4$ was wrapped by PG. Importantly, it further suggests that PG was doped with N element, which can induce more defect and dipole relaxation.[19]

Fig. 4a–d illustrates the complex permittivity ($\varepsilon_r = \varepsilon' - j\varepsilon''$) and complex permeability ($\mu_r = \mu' - j\mu''$) of $CoFe_2O_4$ and PG/$CoFe_2O_4$ composite. In general, the real parts (ε' and μ') represents the storage of electromagnetic energy, and the imaginary parts (ε'' and μ'') symbolizes the dissipation of electromagnetic energy.[35] As shown in Fig. 4a and b, the ε' and ε'' values of $CoFe_2O_4$ exhibit slight variation with the change of frequency, ranging from 3.6–3.3 and 0.34–0.16, respectively. As for PG/$CoFe_2O_4$ composite, it shows a declining trend with the increasing frequency, ranging from 7.3–4.9 and 2.72–1.55, respectively. Obviously, compared to $CoFe_2O_4$, the ε' and ε'' values of PG/$CoFe_2O_4$ increase significantly in the whole frequency. In Fig. 4c and d, the μ' values decrease with the changing frequency and the μ'' values present some fluctuations for both $CoFe_2O_4$ and PG/$CoFe_2O_4$. And owing to the adding of nonmagnetic PG, the μ'' value of PG/$CoFe_2O_4$ is lower than that of $CoFe_2O_4$ in the entire frequency. Further, the corresponding dielectric loss tangent (tan $\delta_\varepsilon = \varepsilon''/\varepsilon'$) and magnetic loss tangent (tan $\delta_\mu = \mu''/\mu'$) are shown in Fig. 4e and f. It suggests that tan δ_ε
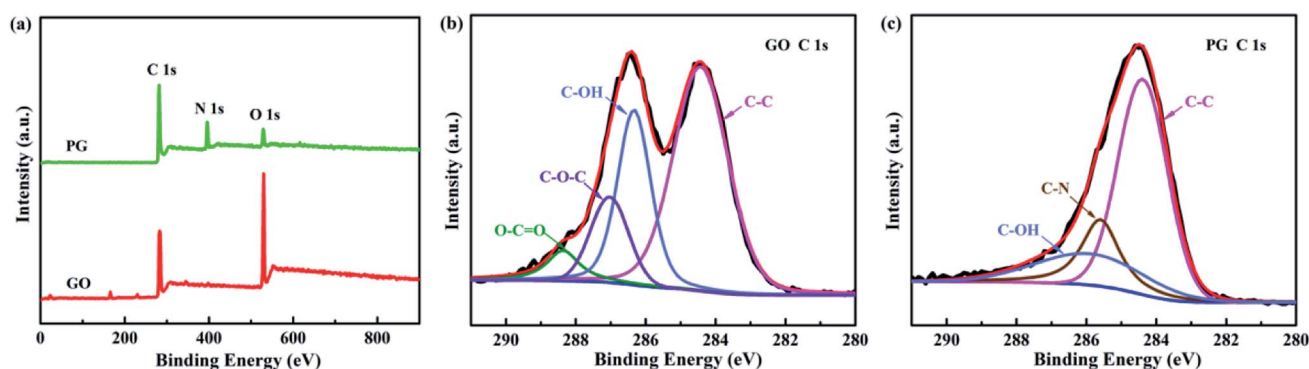

Fig. 2 (a) XPS survey spectra of GO and PG, high-resolution C 1s spectra of (b) GO and (c) PG.
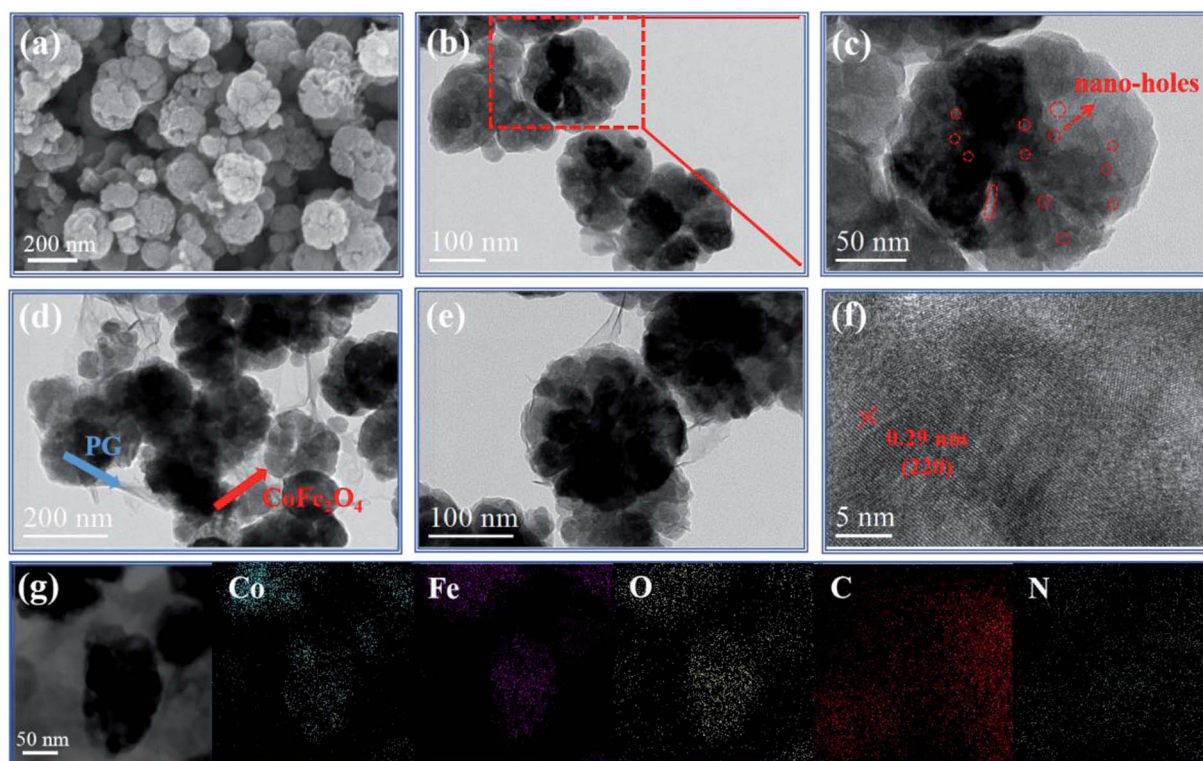
Fig. 3 SEM image of (a) $CoFe_2O_4$, TEM images of (b and c) $CoFe_2O_4$ and (d and e) $PG/CoFe_2O_4$ composite, (f) HRTEM image and (g) elemental mapping distribution of $PG/CoFe_2O_4$ composite.
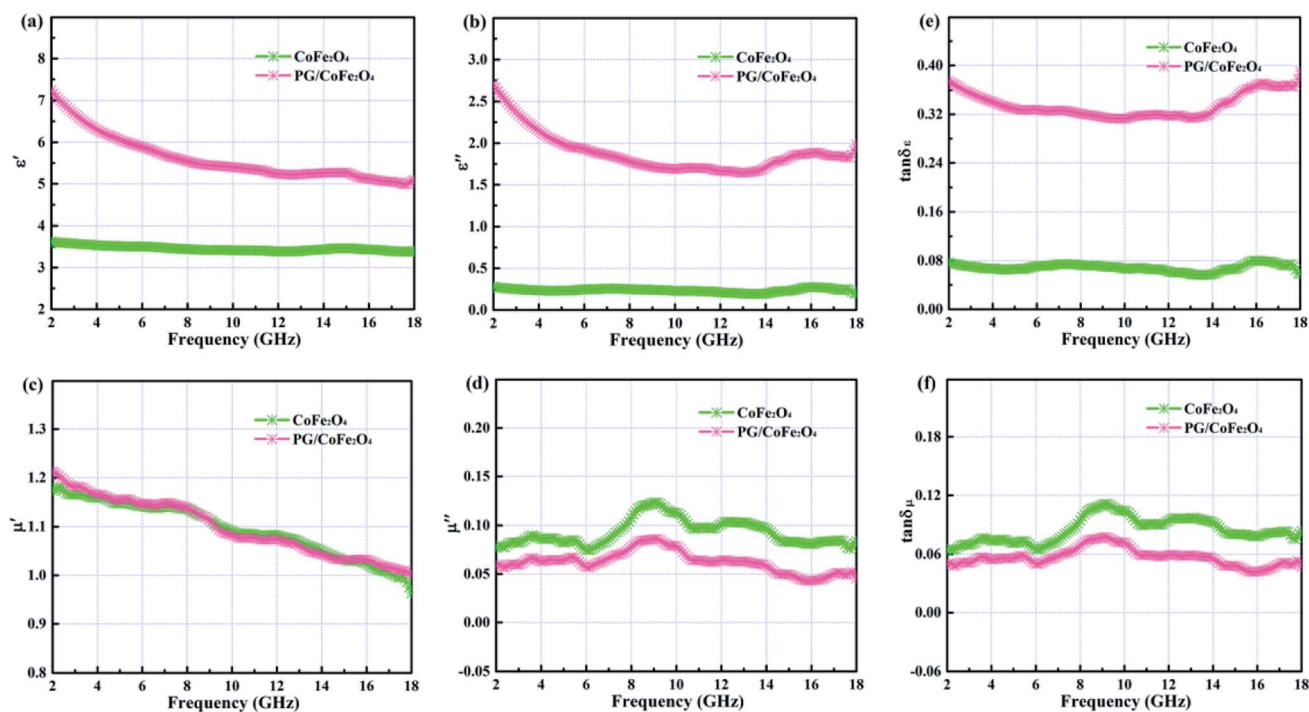

Fig. 4 Frequency dependence of (a) real part and (b) imaginary part of permittivity, (c) real part and (d) imaginary part of permeability, (e) dielectric loss tangent and (f) magnetic loss tangent of $CoFe_2O_4$ and $PG/CoFe_2O_4$ composite.
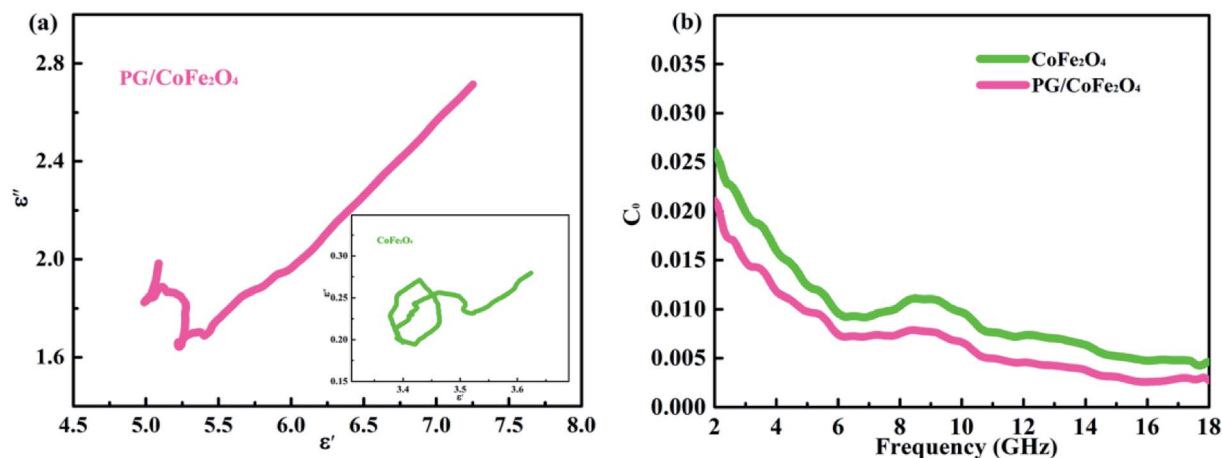
Fig. 5 (a) The $\varepsilon'-\varepsilon''$ plots and (b) C_0-f curves of CoFe$_2$O$_4$ and PG/CoFe$_2$O$_4$ composite.

value increases greatly and tan δ_μ value decreases slightly with the introduction of PG. And the value of tan δ_ε is much larger that tan δ_μ in the whole frequency for PG/CoFe$_2$O$_4$, confirming that the dielectric loss plays a dominant role in MA for PG/CoFe$_2$O$_4$ composite.

The dielectric loss of an absorber generally associates with conductive loss and polarization relaxation.[36] In terms of conductive loss, based on free electron theory ($\sigma = \varepsilon_0\varepsilon''2\pi f$), the higher conductivity (σ) leads to larger dielectric imaginary parts (ε''), and further increases dielectric loss.[37] Herein, the introduction of PG greatly enhances the conductivity of PG/CoFe$_2$O$_4$ composite, hence its dielectric loss is significantly improved compared to CoFe$_2$O$_4$. With regard to polarization relaxation, interfacial polarization and dipole polarization are usually considered in microwave frequency range.[38] According to Debye relaxation theory, the plot of $\varepsilon'-\varepsilon''$ is a single semicircle (Cole–Cole semicircle) and each semicircle stands for a Debye relaxation process.[39] As shown in Fig. 5a, both samples present more than one imperfect semicircle, indicating multiple Debye relaxation processes. The multiple interfaces between CoFe$_2$O$_4$ and PG, cavities of CoFe$_2$O$_4$ microsphere will induce abundant interfacial polarization. Moreover, the structural defects, nitrogen-doping and residual group of PG can act as polarization center to generate dipole polarization.[19,20] In addition, the long line tail of

plot for PG/CoFe$_2$O$_4$ further confirms the conductive loss due to introduction of PG.[40]

The magnetic loss is composed of hysteresis loss, domain-wall resonance, exchange resonance, eddy current loss and natural resonance.[24] In microwave band, it mainly attributed to eddy current loss, natural and exchange resonance.[22,36] The eddy current loss can be expressed as $C_0 = \mu''(\mu')^{-2}f^{-1} = 2\pi\mu_0\sigma d^2/3$.[41,42] If magnetic loss only derive from eddy current effect, the C_0 will be a constant in the whole frequency. As shown in Fig. 5b, the values of C_0 are changeable for both samples, especially in 2–6 GHz. This result suggests that magnetic loss is caused by eddy current loss, natural resonance (2–6 GHz) and exchange resonance (exceed 6 GHz) jointly.

The reflection loss can be assessed by transmission line theory and is given as follows:[43]

$$\text{RL (dB)} = 20 \log|(Z_{\text{in}} - Z_0)/(Z_{\text{in}} + Z_0)| \qquad (1)$$

$$Z_{\text{in}} = Z_0(\mu_r/\varepsilon_r)^{1/2} \tanh[j(2\pi fd/c)(\mu_r \times \varepsilon_r)^{1/2}] \qquad (2)$$

where Z_{in} represents input impedance of absorber, Z_0 is impedance of free space, f is frequency of microwave, d is thickness of absorber, c is velocity of light in free space.
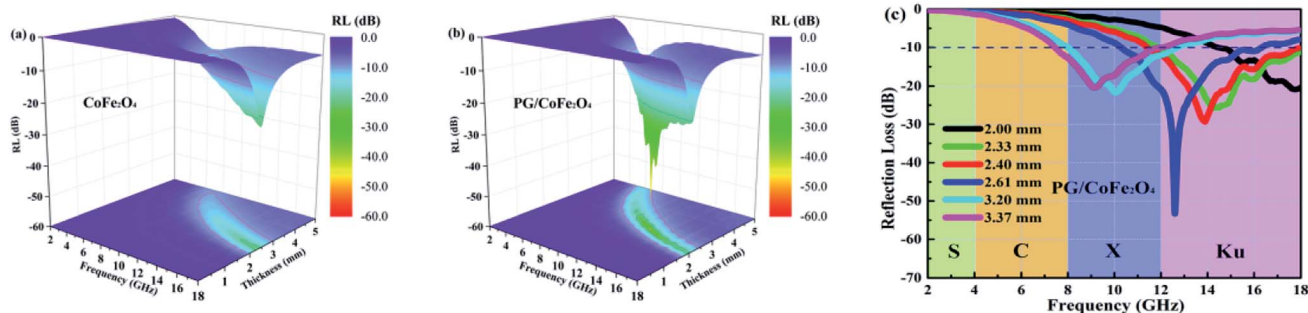

Fig. 6 Frequency dependence of RL with different thickness for (a) CoFe$_2$O$_4$ and (b and c) PG/CoFe$_2$O$_4$ composite.

Table 1 Comparative MA performance of some graphene-based absorbers

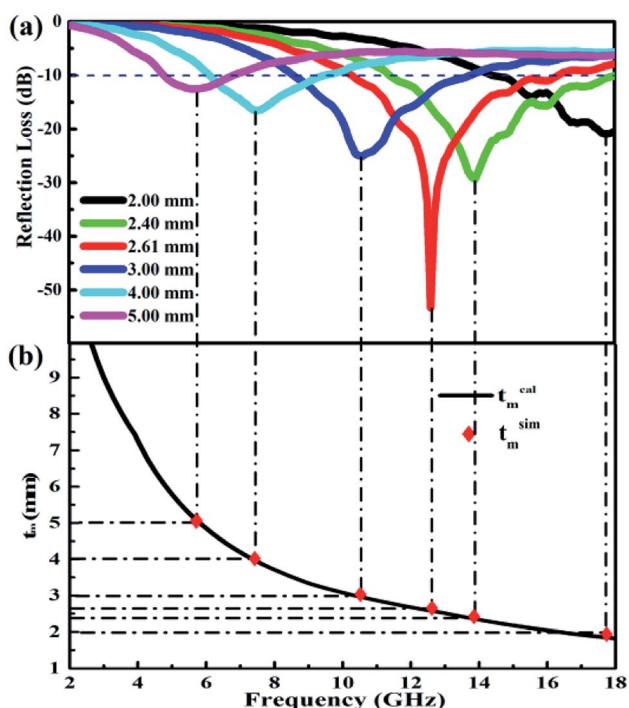| Absorber	RL_{max} (dB)	EAB (GHz)	Thickness (mm)	Ref.
Fe-doped SnO_2/rGO	−29.0	2.7	5.30	44
Graphene/SiC	−37.1	2.2	2.60	45
$Ti_3C_2T_x$@rGO	−31.2	5.4	2.05	46
$BiFeO_3$/rGO	−46.7	4.7	1.80	47
N/B_{12}-rGO	−52.0	6.0	2.80	48
PANI/GA	−42.3	3.2	3.00	49
γ-Fe_2O_3/PNG	−40.18	3.41	2.50	50
PG/$CoFe_2O_4$	−53.3	6.0	2.61	This work
PG/$CoFe_2O_4$	−29.3	6.6	2.40	This work

Fig. 7 Frequency dependence of (a) RL with different thickness, and (b) the t_m−f_m curve of PG/$CoFe_2O_4$ composite.

Fig. 6a–c depicts the frequency-dependent RL curves of $CoFe_2O_4$ and PG/$CoFe_2O_4$ with different thickness. For $CoFe_2O_4$ shown in Fig. 6a, the RL_{max} is −22.5 dB at 18.0 GHz with EAB (RL less than −10 dB) of 3.8 GHz (14.2–18.0 GHz) for the thickness of 2.32 mm. It indicates that pure $CoFe_2O_4$ exhibits poor MA performance. For PG/$CoFe_2O_4$ shown in Fig. 6b and c, the RL_{max} value of −53.3 dB at 2.61 mm and the corresponding EAB of 6.0 GHz (10.3–16.3 GHz). Moreover, when thickness of 2.40 mm, the ultra-broad bandwidth attains 6.6 GHz (11.4–18.0 GHz), covering the whole K_u band. And the EAB is 4.7 GHz (8.0–12.7 GHz) at 3.20 mm, which can completely cover the X band. Additionally, the comparative MA performance of some graphene-based absorbers is summarized in Table 1. Obviously, the PG/$CoFe_2O_4$ composite

exhibits preferable MA performance with both strong absorption and wide bandwidth.

Noticeably, the frequency associated with RL_{max} exhibits a lower trend with the increasing thickness. This phenomenon can be explained by quarter-wavelength ($\lambda/4$) cancellation model with following equation:[51]

$$t_m = \frac{n\lambda}{4} = \frac{nc}{4f_m\sqrt{|\varepsilon_r \mu_r|}} \quad (n = 1, 3, 5...) \quad (3)$$

where t_m and f_m represent the thickness of absorber and peak frequency, respectively. In Fig. 7, the simulated matching thickness (t_m^{sim}) are well agreed with calculated matching thickness (t_m^{cal}) based on above model. Thus, this model can provide instruction for thickness adjustment of absorber with different frequency.

An excellent absorber should simultaneously fulfill two requirements, including strong attenuation capacity and favorable impedance matching. Generally, the attenuation constant (α) is used to assess attenuation capacity of absorber and it can be expressed as follows:[52]

$$\alpha = \frac{\sqrt{2}\pi f}{c}\sqrt{(\mu''\varepsilon'' - \mu'\varepsilon') + \sqrt{(\mu''\varepsilon'' - \mu'\varepsilon')^2 + (\varepsilon'\mu'' + \varepsilon''\mu')^2}} \quad (4)$$

As shown in Fig. 8a, the α value of PG/$CoFe_2O_4$ is larger than $CoFe_2O_4$ in the whole frequency, suggesting the strong attenuation ability of PG/$CoFe_2O_4$. Meanwhile, normalized characteristic impedance ($Z = |Z_{in}/Z_0|$) is applied to evaluate the transmission behaviors of microwave. The $Z = 1$ means all incident microwaves enter into absorber without reflection.[53] As presented in Fig. 8b, the Z value is closer to 1 in most of frequency range for PG/$CoFe_2O_4$ at 2.61 mm, which is much better than that of $CoFe_2O_4$. Therefore, the impedance matching of composite is improved by introducing PG. The PG/$CoFe_2O_4$ composite possesses higher attenuation capacity and superb impedance matching, leading to excellent MA performance.

The MA mechanism of PG/$CoFe_2O_4$ composite is elaborated in Fig. 9. The superb MA performance can be ascribed to uniquely hierarchical porous structure, synergistic effects of dielectric loss (conductive loss, interface and dipole polarization) and magnetic loss (eddy current loss, natural and exchange resonance). Firstly, the PG nanosheets establish a conductive network to generate conductive loss. Secondly, the structural defects, nitrogen-doping and residual group of PG can produce dipole polarization. Thirdly, abundant interfaces between $CoFe_2O_4$ and PG create interface polarization, adjacent layers of PG and cavities of $CoFe_2O_4$ can generate multiple reflection. Fourthly, the $CoFe_2O_4$ microspheres induce eddy current loss, natural and exchange resonance. Lastly, the appropriate dielectric and magnetic loss facilitate good impedance matching. Therefore, the PG/$CoFe_2O_4$ composite exhibits excellent MA performance.
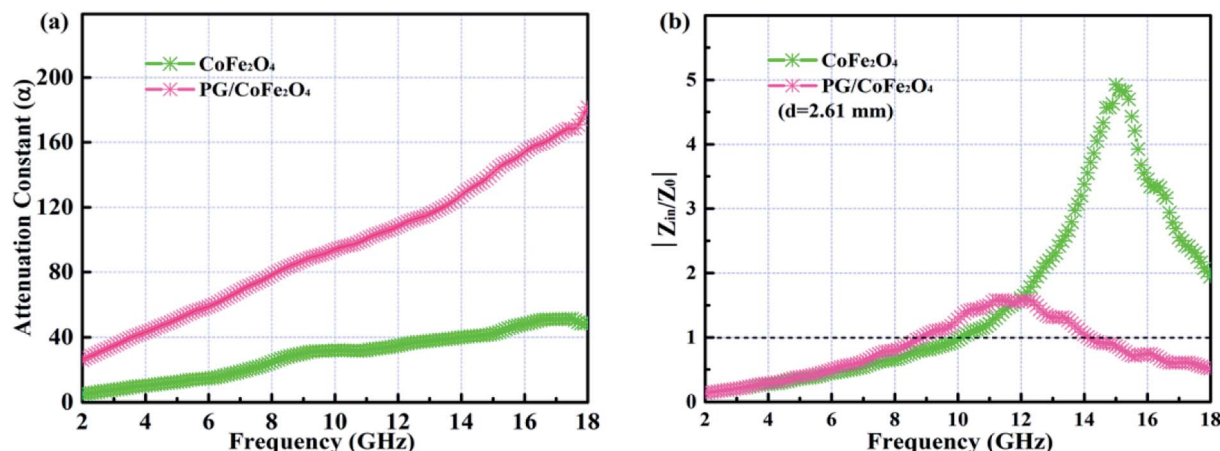
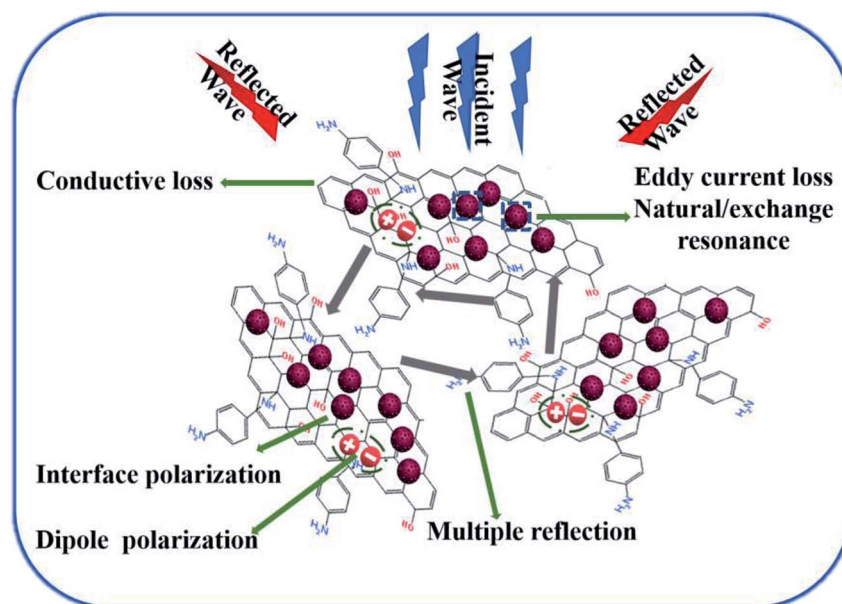Fig. 8 Frequency dependence of (a) attenuation constant α and (b) normalized characteristic impedance Z at 2.61 mm of PG/CoFe$_2$O$_4$ composite.

Fig. 9 Schematic illustration of MA mechanism of PG/CoFe$_2$O$_4$ composite.

4. Conclusions

In summary, the hierarchical PG/CoFe$_2$O$_4$ binary hybrid was prepared by using PPD to functionalize and reduce GO. Owing to the introduction of PG, the PG/CoFe$_2$O$_4$ composite present superb MA performance than pure CoFe$_2$O$_4$. The strong RL$_{max}$ of -53.3 dB and the ultra-broad bandwidth attains 6.6 GHz from 11.4 to 18.0 GHz at 2.40 mm, which completely covered the K_u band. When thickness of 3.20 mm, the EAB was 4.7 GHz (8.0–12.7 GHz), which covered the whole X band. This functional binary composite has great potential to be used in MA field and even in other fields.

Conflicts of interest

There are no conflicts to declare.

Acknowledgements

References

1 L. Wang, Y. Huang, X. Sun, H. Huang, P. Liu, M. Zong and Y. Wang, *Nanoscale*, 2014, **6**, 3157–3164.
2 Z. Zhao, S. Xu, Z. Du, C. Jiang and X. Huang, *ACS Sustainable Chem. Eng.*, 2019, **7**, 7183–7192.

3 X. Zhang, X. Zhang, H. Yuan, K. Li, Q. Ouyang, C. Zhu, S. Zhang and Y. Chen, *Chem. Eng. J.*, 2020, **383**, 123208.

4 M. Zhang, Z. Jiang, H. Si, X. Zhang, C. Liu, C. Gong, Y. Zhang and J. Zhang, *Phys. Chem. Chem. Phys.*, 2020, **22**, 8639–8646.

5 S. Zhao, C. Wang and B. Zhong, *J. Magn. Magn. Mater.*, 2020, **495**, 165753.

6 G. Wen, X. Zhao, Y. Liu, H. Zhang and C. Wang, *Chem. Eng. J.*, 2019, **372**, 1–11.

7 N. Zhang, Y. Huang and M. Wang, *J. Colloid Interface Sci.*, 2018, **530**, 212–222.

8 J. Li, D. Zhou, W.-F. Liu, J.-Z. Su and M.-S. Fu, *Scr. Mater.*, 2019, **171**, 42–46.

9 W. Xu, G.-S. Wang and P.-G. Yin, *Carbon*, 2018, **139**, 759–767.

10 H.-B. Zhao, J.-B. Cheng, J.-Y. Zhu and Y.-Z. Wang, *J. Mater. Chem. C*, 2019, **7**, 441–448.

11 J. Feng, Y. Zong, Y. Sun, Y. Zhang, X. Yang, G. Long, Y. Wang, X. Li and X. Zheng, *Chem. Eng. J.*, 2018, **345**, 441–451.

12 W. Shen, B. Ren, K. Cai, Y.-F. Song and W. Wang, *J. Alloys Compd.*, 2019, **774**, 997–1008.

13 S. Wang, Y. Xu, R. Fu, H. Zhu, Q. Jiao, T. Feng, C. Feng, D. Shi, H. Li and Y. Zhao, *Nano-Micro Lett.*, 2019, **11**, 76.

14 J. Li, H. Ji, Y. Xu, J. Zhang and Y. Yan, *J. Mater. Res. Technol.*, 2020, **9**, 762–772.

15 R. Shu, G. Zhang, J. Zhang, X. Wang, M. Wang, Y. Gan, J. Shi and J. He, *J. Alloys Compd.*, 2018, **736**, 1–11.

16 H.-L. Ma, H.-B. Zhang, Q.-H. Hu, W.-J. Li, Z.-G. Jiang, Z.-Z. Yu and A. Dasari, *ACS Appl. Mater. Interfaces*, 2012, **4**, 1948–1953.

17 B. Song, J. Choi, Y. Zhu, Z. Geng, L. Zhang, Z. Lin, C. Tuan, K. Moon and C. Wong, *Chem. Mater.*, 2016, **28**, 9110–9121.

18 H. Yuan, F. Yan, C. Li, C. Zhu, X. Zhang and Y. Chen, *ACS Appl. Mater. Interfaces*, 2018, **10**, 1399–1407.

19 Y. Wang, X. Gao, X. Wu, W. Zhang, C. Luo and P. Liu, *Chem. Eng. J.*, 2019, **375**, 121942.

20 R. Shu, J. Zhang, C. Guo, Y. Wu, Z. Wan, J. Shi, Y. Liu and M. Zheng, *Chem. Eng. J.*, 2020, **384**, 123266.

21 Y. Ren, S. Li, B. Dai and X. Huang, *Appl. Surf. Sci.*, 2014, **311**, 1–4.

22 T. Zhu, S. Chang, Y.-F. Song, M. Lahoubi and W. Wang, *Chem. Eng. J.*, 2019, **373**, 755–766.

23 J. He, S. Liu, L. Deng, D. Shan, C. Cao, H. Luo and S. Yan, *Appl. Surf. Sci.*, 2020, **504**, 144210.

24 X. Wang, T. Zhu, S. Chang, Y. Lu, W. Mi and W. Wang, *ACS Appl. Mater. Interfaces*, 2020, **12**, 11252–11264.

25 Y. Li, M. Yuan, H. Liu and G. Sun, *J. Alloys Compd.*, 2020, **826**, 154147.

26 L. Huang, J. Li, Z. Wang, Y. Li, X. He and Y. Yuan, *Carbon*, 2019, **143**, 507–516.

27 A. Feng, T. Hou, Z. Jia and G. Wu, *RSC Adv.*, 2020, **10**, 10510–10518.

28 T. Ma, Y. Cui, Y. Sha, L. Liu, J. Ge, F. Meng and F. Wang, *Synth. Met.*, 2020, **265**, 116407.

29 A. A. Ibrahim, A. Lin, M. S. Adly and M. S. El-Shall, *J. Catal.*, 2020, **385**, 194–203.

30 X.-J. Zhang, G.-S. Wang, W.-Q. Cao, Y.-Z. Wei, J.-F. Liang, L. Guo and M.-S. Cao, *ACS Appl. Mater. Interfaces*, 2014, **6**, 7471–7478.

31 Y. Lei, Z. Yao, H. Lin, A. A. Haidry, J. Zhou and P. Liu, *Mater. Lett.*, 2019, **236**, 456–459.

32 A. Wang, L. Cheng, X. Chen, W. Zhao, C. Li, W. Zhu and D. Shang, *Dyes Pigm.*, 2019, **160**, 344–352.

33 F. Yan, Y. Zong, C. Zhao, G. Tan, Y. Sun, X. Li, Z. Ren and X. Zheng, *J. Alloys Compd.*, 2018, **742**, 928–936.

34 Z. Xiang, J. Xiong, B. Deng, E. Cui, L. Yu, Q. Zeng, K. Pei, R. Che and W. Lu, *J. Mater. Chem. C*, 2020, **8**, 2123–2134.

35 L. Liang, Z. Zhang, F. Song, W. Zhang, H. Li, J. Gu, Q. Liu and D. Zhang, *Carbon*, 2020, **162**, 283–291.

36 H. Zhao, Y. Cheng, Y. Zhang, Z. Zhang, L. Zhou and B. Zhang, *Dalton Trans.*, 2019, **48**, 15263–15271.

37 B. Mordina, R. Kumar, R. K. Tiwari, D. K. Setua and A. Sharma, *J. Phys. Chem. C*, 2017, **121**, 7810–7820.

38 M. Zeng, Q. Cao, J. Liu, B. Guo, X. Hao, Q. Liu, X. Liu, X. Sun, X. Zhang and R. Yu, *ACS Appl. Mater. Interfaces*, 2020, **12**, 1222–1231.

39 S. Wang, S. Peng, S. Zhong and W. Jiang, *J. Mater. Chem. C*, 2018, **6**, 9465–9474.

40 H. Wang, F. Meng, F. Huang, C. Jing, Y. Li, W. Wei and Z. Zhou, *ACS Appl. Mater. Interfaces*, 2019, **11**, 12142–12153.

41 X. Zhang, J. Xu, X. Liu, S. Zhang, H. Yuan, C. Zhu, X. Zhang and Y. Chen, *Carbon*, 2019, **155**, 233–242.

42 J. Liu, H. Liang and H. Wu, *Composites, Part A*, 2020, **130**, 105760.

43 Y. Cheng, Y. Zhao, H. Zhao, H. Lv, X. Qi, J. Cao, G. Ji and Y. Du, *Chem. Eng. J.*, 2019, **372**, 390–398.

44 J. Zhang, R. Shu, Y. Ma, X. Tang and G. Zhang, *J. Alloys Compd.*, 2019, **777**, 1115–1123.

45 X. Li, Z. Li, L. Que, Y. Ma, L. Zhu and C. Pei, *J. Alloys Compd.*, 2020, **835**, 155172.

46 L. Wang, H. Liu, X. Lv, G. Cui and G. Gu, *J. Alloys Compd.*, 2020, **828**, 154251.

47 X. Gao, Y. Wang, Q. Wang, X. Wu, W. Zhang, M. Zong and L. Zhang, *Ceram. Int.*, 2019, **45**, 3325–3332.

48 Z. Sun, Z. Yan, K. Yue, A. Li and L. Qian, *Composites, Part B*, 2020, **196**, 108132.

49 Y. Wang, X. Gao, Y. Fu, X. Wu, Q. Wang, W. Zhang and C. Luo, *Composites, Part B*, 2019, **169**, 221–228.

50 S. Wang, Q. Jiao, Q. Shi, H. Zhu, T. Feng, Q. Lu, C. Feng, H. Li, D. Shi and Y. Zhao, *Ceram. Int.*, 2020, **46**, 1002–1010.

51 R. Wang, M. He, Y. Zhou, S. Nie, Y. Wang, W. Liu, Q. He, W. Wu, X. Bu and X. Yang, *ACS Appl. Mater. Interfaces*, 2019, **11**, 38361–38371.

52 L. Liang, G. Han, Y. Li, B. Zhao, B. Zhou, Y. Feng, J. Ma, Y. Wang, R. Zhang and C. Liu, *ACS Appl. Mater. Interfaces*, 2019, **11**, 25399–25409.

53 J. Xiong, Z. Xiang, B. Deng, M. Wu, L. Yu, Z. Liu, E. Cui, F. Pan, R. Liu and W. Lu, *Appl. Surf. Sci.*, 2020, **513**, 145778.